Finite element modeling of nanoindentation on C–S–H: Effect of pile-up and contact friction

E. Sarris [a], G. Constantinides [a,b],*

[a] Research Unit for Nanostructured Materials Systems, Department of Mechanical Engineering and Materials Science and Engineering, Cyprus University of Technology, Lemesos, Cyprus
[b] Department of Civil and Environmental Engineering, Massachusetts Institute of Technology, Cambridge, MA, USA

ARTICLE INFO

ABSTRACT

In this paper we computationally study the indentation response of a rigid axisymmetric indenter on a semi-infinite elasto-plastic material of the Mohr–Coulomb type. The finite element method is used to quantify the effect of material properties (E, c, φ) and contact friction (μ) on the indentation response of C–S–H phases. The high E/c-ratio for both C–S–H phases, together with their cohesive-frictional behavior, leads to pile-up phenomena around the penetrated probe. The influence of all these parameters on the actual area of contact and its subsequent effect on commonly extracted quantities of the indentation test, namely indentation modulus (M) and indentation hardness (H), is investigated. It is shown that contact friction affects the contact area between the indenter and indented material and as a consequence interferes, to a certain extent, with the procedure for estimating elastic and plastic material properties. The effect is more pronounced for the hardness measurements.

1. Introduction

Instrumented indentation had evolved into a standardized method for testing the mechanical properties of small volumes [1,2]. It was initially developed for metals and hard thin films and the analysis therefore concentrated on constitutive material laws that are pressure insensitive and follow a yield criterion of the Tresca or Von-Mises type. The effect of the hydrostatic pressure on the plasticity response, that many materials – including cementitious materials, soils – exhibit, has been generally neglected from the indentation analysis [3–6]. Furthermore, the contact friction between the indenter and the material [7–10] has not been accounted for, neither in experiments [11–17] nor in simulations [18–20] of cementitious materials. In this paper, the finite element method is used to simulate a nanoindentation test on a cohesive-frictional material of the Mohr–Coulomb type, representing the C–S–H phase (Fig. 1a), and the loading–unloading responses (Fig. 1b) are studied in detail. The effect of material properties (E, c, φ) and contact friction (μ) on the commonly extracted quantities of the indentation test, namely indentation modulus (M) and indentation hardness (H), is investigated.

2. Materials and methods

2.1. C–S–H properties and model parameters

Calcium silicate hydrate, or in short C–S–H, is the dominant volumetric component of all cementitious systems, and as a consequence it drives their macroscopic response. The dimensions of this phase are usually restricted in the micrometer size and as a consequence it makes it difficult for traditional tests, such as uni-axial compression and tension to be employed. Their mechanical response has therefore only been probed with the advent of nano-indentation that allowed measurements to be performed at the level and environment that C–S–H naturally occurs [11]. Due to the heterogeneous nature of cementitious materials, statistical techniques need to be employed such as the property of each phase is identified [21]. A low density (LD C–S–H) and a high density (HD C–S–H) version have been reported [22]. Furthermore, the two C–S–H phases exhibit pressure-sensitive plastic behavior that could be approximated to first order by a Mohr–Coulomb criterion in which the critical shear strength τ is expressed in terms of the normal strength σ through: $\tau = c + \sigma \tan(\varphi)$. Estimates of the elastic and plastic properties of the two types of C–S–H have been obtained in Ref. [23]: LD C–S–H (E = 21 GPa, c = 50 MPa, φ = 12°) and HD C–S–H (E = 31 GPa, c = 97 MPa, φ = 12°).

* Corresponding author at: Research Unit for Nanostructured Materials Systems, Department of Mechanical Engineering and Materials Science and Engineering, Cyprus University of Technology, Lemesos, Cyprus.
E-mail addresses: ernestos.sarris@cut.ac.cy (E. Sarris), george_c@mit.edu, g.con stantinides@cut.ac.cy (G. Constantinides).
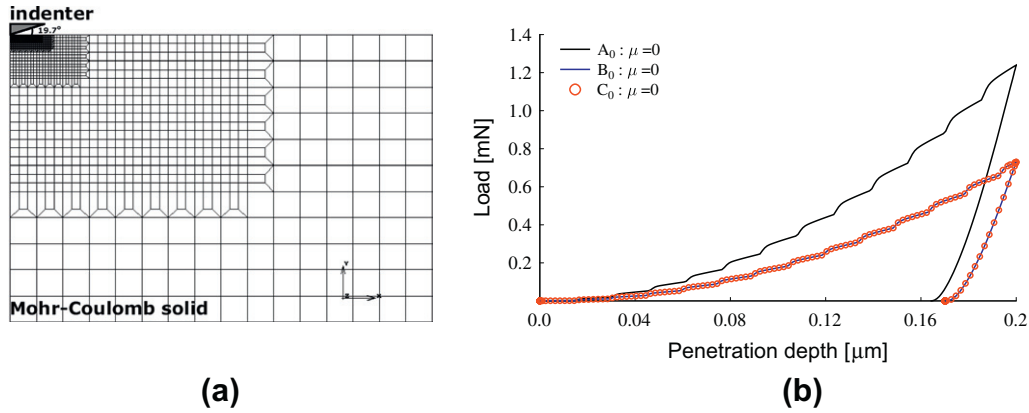
Fig. 1. (a) Geometrical details and finite element mesh of the studied problem. (b) Resulting force versus penetration depth curves of simulated indentation on the three model materials, frictionless LD (A0), HD C–S–H (B0) and a model material (C0).

2.2. Indentation mechanics

A typical nanoindentation test consists of establishing contact between an indenter and a sample, while continuously monitoring the load P and the penetration depth h. Analysis of the P–h response proceeds by applying a continuum scale model to derive the indentation modulus M and the indentation hardness H [1,2]:

$$M = \frac{\sqrt{\pi}}{2} \frac{S}{\sqrt{A}} \tag{1}$$

$$H = \frac{P_{\max}}{A} \tag{2}$$

where S is the unloading slope evaluated at maximum indentation depth $h_{\max}$ $\left(S = \frac{dP}{dh}\big|_{h_{\max}}\right)$, $P_{\max}$ is the maximum indentation force, and A is the projected area of contact at $h_{\max}$. Eq. (1) has its basis on the frictionless elastic indentation solution and suggests that the elastic properties of the material can be extracted through:

$$\frac{1}{M} = \frac{(1 - v_s^2)}{E_s} + \frac{(1 - v_i^2)}{E_i} \tag{3}$$

where the subscripts i and s indicate indenter and sample respectively. In the case of a rigid indenter the second term in the right hand side of Eq. (3) vanishes. An estimate of the effect of friction can be incorporated in Eq. (1) by utilizing the linear elastic solution for adhesive (no-slip) indentation [7,8]. Eq. (1) is corrected to account for an additional coefficient which includes the adhesive effects and provides an upper bound to the frictional contact problem:

$$\frac{E_s}{(1 - v_s^2)} = C \frac{\sqrt{\pi}}{2} \frac{S}{\sqrt{A}} \tag{4}$$

where C has been calculated analytically in [7] and equals to $C = \frac{(1-v)}{(1-2v)} \ln(3 - 4v)$. This correction factor suggests deviations on the order of 5–10% for materials with Poisson's ratio in the range of 0–0.5. Nevertheless, inaccuracies included in the analysis due to improper area estimation are not explicitly included and will be the subject of our discussion in the following section.

2.3. Finite element modeling

Two dimensional axisymmetric finite element simulations are performed to investigate the effect of friction on the indentation response of C–S–H. The indenter was modeled as a rigid cone with half apex angle θ of 70.3°. This conical angle ensures the same contact depth-projected area of contact relation as in Vickers and

Berkovich pyramidal indenters. Details of the model geometry are shown in Fig. 1. The 'semi-infinite' half space is modeled as a $250 \times 250\ \mu m^2$ domain. This continuum space is discretized using 4-node axisymmetric, isoparametric element (CAX4-full integration). The element size was continuously refined as approaching the indenter contact region for greater accuracy. This was performed in four steps, with the final domain having square element of 50 nm. A mesh sensitivity analysis was performed to ensure that the simulations results were insensitive to the mesh size in the indenter region.

Frictional effects in the indenter–material interface were included in the analysis through an isotropic Coulomb model, in which the local shear stress τ_c is related to the local normal pressure p_c through $\tau_c = \mu p_c$ where μ is the friction coefficient between the indenter and the surface. We assume that the loading rate is slow enough such as static friction can securely model the interface response. Simulations proceeded in two steps. The indenter was firstly subjected to a ramped vertical displacement, followed by an indenter retraction to the original position which corresponded to complete unloading at zero load. During this process the lower edge of the material was constrained vertically. Axisymmetric boundary conditions were used along the symmetry axis beneath the indenter.

3. Results and discussion

3.1. P–h curves

Dimensional analysis suggests that the loading portion of the curve will be a function of E/c, φ, v, and μ:

$$\frac{P}{ch^2} = \Im\left(\frac{E}{c}, \mu, v\right) \tag{5}$$

Fig. 1b shows the P–h curves of the two types of C–S–H (A0 and B0) for the frictionless case ($\mu = 0$). Based on Eq. (5) the difference can be attributed to the difference in the E/c-ratio, given the fact that φ, v, and μ are the same. To test the scaling relation of Eq. (5) we performed a simulation on a model material (C0) with the same E/c-ratio as LD C–S–H (A0) but with doubled E and c values ($E = 42$ GPa and $c = 100$ MPa, $E/c = 420$). The resulting curve properly scaled by a factor of 2 (due to the doubling of cohesion) completely overlaps the LD C–S–H curve thus verifying the validity of Eq. (5). Indentation tests for all model materials described in Table 1 have been simulated to a maximum indentation depth of 200 nm and the resulting force vs. penetration responses, P–h curves, are presented in Fig. 2. It can be seen that no significant variations in

Table 1
Material properties used for the finite element simulations.

Model name	c (MPa)	φ (°)	E (GPa)	v (−)	E/c (−)	μ (−)
LD C–S–H						
A0	50	12	21	0.24	420	0
A1	50	12	21	0.24	420	0.125
A2	50	12	21	0.24	420	0.250
A3	50	12	21	0.24	420	0.500
A4	50	12	21	0.24	420	1.000
HD C–S–H						
B0	97	12	31	0.24	320	0
B1	97	12	31	0.24	320	0.125
B2	97	12	31	0.24	320	0.250
B3	97	12	31	0.24	320	0.500
B4	97	12	31	0.24	320	1.000
C0	100	12	42	0.24	420	0

their overall response are observed in relation to the magnitude of the interface friction. Individual characteristics for all curves have been extracted and tabulated in Table 2, such as to investigate the response in more details. In particular, the maximum force P_{max}, unloading slope at maximum depth S, the projected area of contact at maximum load A, elastic modulus E, and hardness H, that there will be discussed in more detailed in the sections below, have been monitored or calculated. While minor, at this particular depth of penetration, there appears to be small variations in the required force to penetrate the LD C–S–H (Fig. 2a) and HD C–S–H (Fig. 2b) to a depth of 200 nm (see Table 2). Furthermore, the unloading slope reduces as the friction coefficient increases: the respective values for the LD C–S–H and HD C–S–H are 0.0335/0.0302/0.0290/0.0287/0.0291 and 0.0460/0.0423/0.0391/0.0388/0.392 as the friction coefficient gradually changes from 0.0 to 1.0.
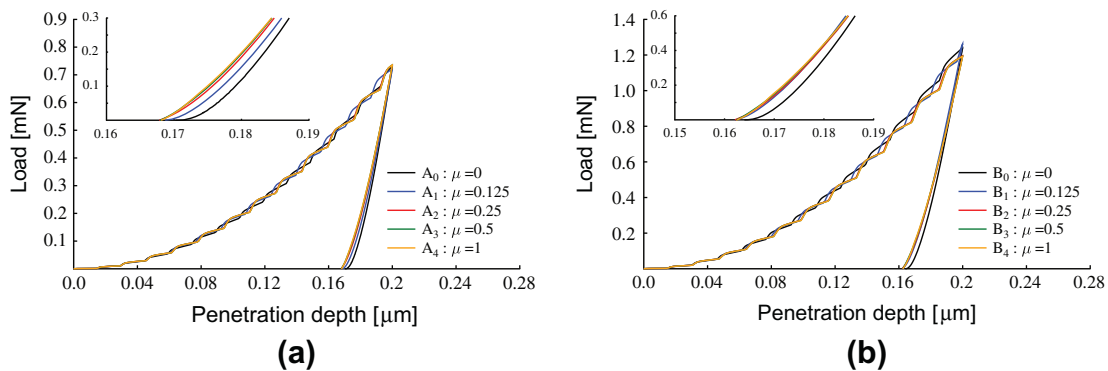
This reduction in S is in line with the analytical solution of adhesive contact and Eq. (4). It should be noted that the unloading slope is included in the indentation modulus calculations (Eq. (1)) and also in the Oliver and Pharr method for estimating the projected area of contact at maximum load, A. The implications of these observations to material properties calculations will be investigated below.

3.2. Area of contact

The projected area of contact at maximum load is an important component for extracting the elastic and plastic properties of the indented material via the indentation modulus and indentation hardness respectively. We therefore wanted to investigate how the presence of contact friction between the indenter and material of interest influences the deformed surface profile and as a consequence the projected area of contact at maximum indentation depth. Fig. 3 shows the deformation profiles of the indented surfaces. The material beneath the indenter tends to pile-up for all materials tested within this study, representing the LD and HD C–S–H phases, and for all friction coefficients. This is in line with recent observations that as the E/c increase the tendency of the material to pile-up is more significant. These observations explain why the LD C–S–H phase with an E/c-ratio of E/c = 420 exhibits more pile-up than the HD C–S–H phase with an E/c = 320. The tendency of the materials to pile-up is amplified by their cohesive-frictional behavior. Fig. 3 shows the deformation profiles of the LD and HD C–S–H for all tested values of contact friction. Shear and normal stresses generated in the interface are plotted in Fig. 4. The rough interface contact between indenter and material generates shear stresses that resist the free slippage which as a consequence leads to a reduction in the pile-up compared with
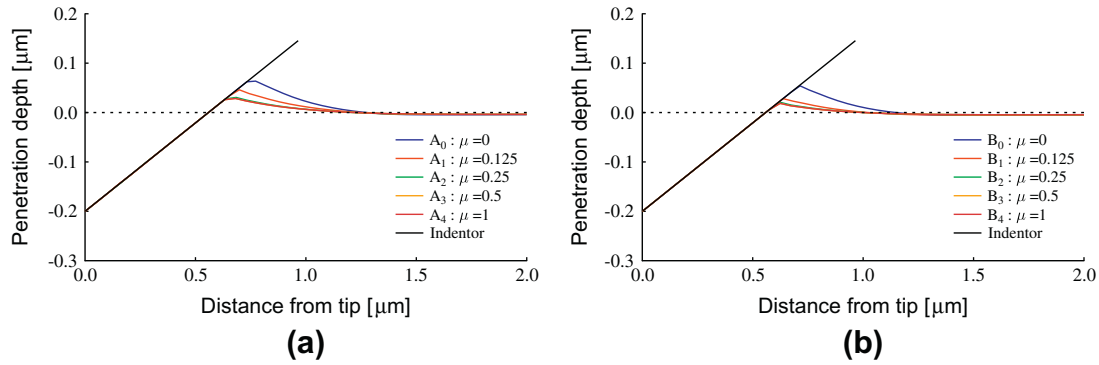
Fig. 2. Effect of contact friction on the simulated indentation force versus penetration depth (P–h responses) of LD and HD C–S–H.

Table 2
Indentation characteristics extracted from the simulated P–h curves. A_{num} stands for the area of contact calculated numerically whereas $A_{O\&P}$ relates to the area of contact estimated through the Oliver and Pharr method.

Model name	P_{max} (mN)	S (N/μm)	$A_{O\&P}$ (μm²)	A_{num} (μm²)	$E_{O\&P}$ (GPa)	E_{num} (GPa)	$H_{O\&P}$ (MPa)	H_{num} (MPa)
LD C–S–H								
A0	0.7307	0.0335	0.9740	1.774	28.37	21.02	750	412
A1	0.7209	0.0302	0.9734	1.435	25.57	21.06	741	502
A2	0.7349	0.0290	0.9730	1.365	24.54	20.72	755	538
A3	0.7356	0.0287	0.9729	1.348	24.30	20.64	756	546
A4	0.7356	0.0291	0.9730	1.347	24.61	20.91	756	546
HD C–S–H								
B0	1.2396	0.0460	0.9725	1.514	38.94	31.21	1275	819
B1	1.2626	0.0423	0.9717	1.366	35.83	30.22	1299	924
B2	1.1959	0.0391	0.9715	1.137	33.13	30.62	1231	1052
B3	1.1933	0.0388	0.9714	1.123	32.88	30.58	1228	1062
B4	1.1930	0.0392	0.9715	1.123	33.21	30.89	1228	1062

Fig. 3. Deformation profiles of the LD and HD C–S–H. A maximum depth of 200 nm is used.
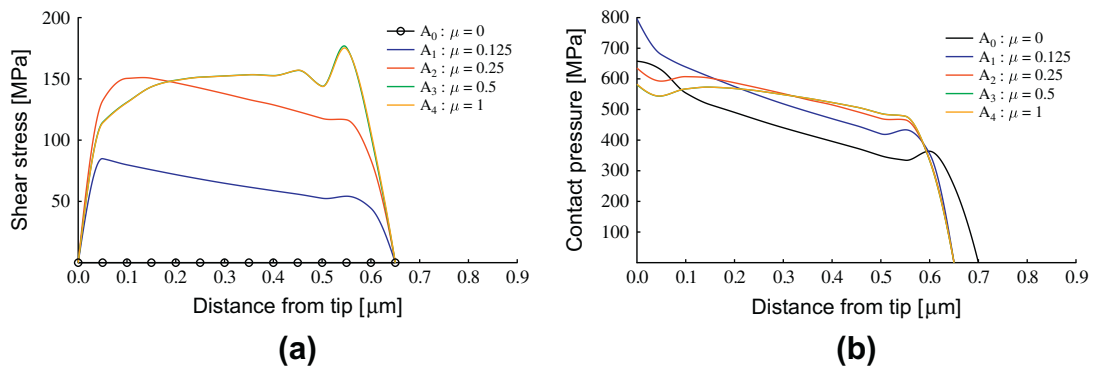

Fig. 4. Effect of contact friction on the distribution of (a) contact shear stress and (b) contact pressure for the LD C–S–H (samples of series A).

the frictionless case. The shear stress distribution increases with increasing μ and tends to flatten for $\mu > 0.25$. We therefore conclude that in contrast to the P–h curves the friction magnitude plays a significant role in the exact contact area that develops between the indenter and the material. This effect cascades into the properties extraction methodologies.

Experimentally the area of contact at maximum load has been traditionally estimated by observing the residual imprint left on the surface of the material after complete load removal. This method, while proven very effective for macroscopic hardness measurements imposed significant complications when performing nanoscale indents. Oliver and Pharr in their seminal paper of 1992 [1] proposed a method in which the area of contact could be estimated by recourse to data extracted directly from the P–h curves thus circumventing the need for nanoscale observations. The contact depth can be estimated using:

$$h_c = h_{max} - \varepsilon \frac{P_{max}}{S} \qquad (6)$$

where ε is a constant that depends on the geometry of the indenter. Important values are: $\varepsilon = 0.72$ for conical probes, $\varepsilon = 0.75$ for a paraboloid of revolution, and $\varepsilon = 1.00$ for flat punches. Based on the observation that the unloading curves are best approximated by an indenter that behaves like a paraboloid of revolution the value of $\varepsilon = 0.75$ is commonly used in practice. The area of contact can then be calculated using an area function $A_c = f(h_c)$ which accounts for any geometric irregularities of the used probe and can be obtained either by multi-depth indentations on a material with known mechanical properties [1], commonly quartz, or by direct observation of the indenter geometry from atomic force microscopy scans [24]. Fig. 5 shows the area of contact for the LD C–S–H (Fig. 5a) and HD C–S–H (Fig. 5b) as predicted by the Oliver and Pharr method ($A_{O\&P}$) and extracted numerically from ABAQUS (A_{num}). As expected, the presence of pile-up phenomena (see Fig. 3) incorporates signif-

icant uncertainty in the area of contact estimation. In fact, the Oliver and Pharr method fails to capture this kind of phenomena with the deviations ($A_{num}/A_{O\&P}$) to even reach a factor of almost 2 in the case of frictionless contact, $\mu = 0$ (A0). As the contact friction increases, discrepancies get less significant, especially for the HD C–S–H with the lower E/c-ratio.

3.3. Indentation modulus

The error in the area of contact estimation propagates into the calculation of the indentation modulus and therefore the elastic moduli of the two types of C–S–H. The presence of friction between the probe and the material activates two competing mechanisms: (a) the reduction of the unloading slope and (b) the reduction in the area of contact due to the restriction of the pile-up phenomena. The implications of these effects on the elastic moduli calculated using numerical methods (E_{num}) and the Oliver and Pharr technique ($E_{O\&P}$) are shown in Fig. 6. The results suggest that when the area of contact is estimated properly (in this case numerically) the elastic properties of the material can be calculated with accuracy (within 3%, see comparison of numerical estimations in Fig. 6 with the straight line – input data). On the other hand, the Oliver and Pharr technique cannot capture the pile-up phenomena properly and can incorporate uncertainty in the elastic modulus calculations, with the deviations ranging from +17% to +35% for the LD C–S–H and +7% to +25% for the HD C–S–H, depending on the friction coefficient, with the highest discrepancy being for the frictionless case.

3.4. Indentation hardness

The miscalculation of the area of contact has significant implications for the indentation hardness determination and as a
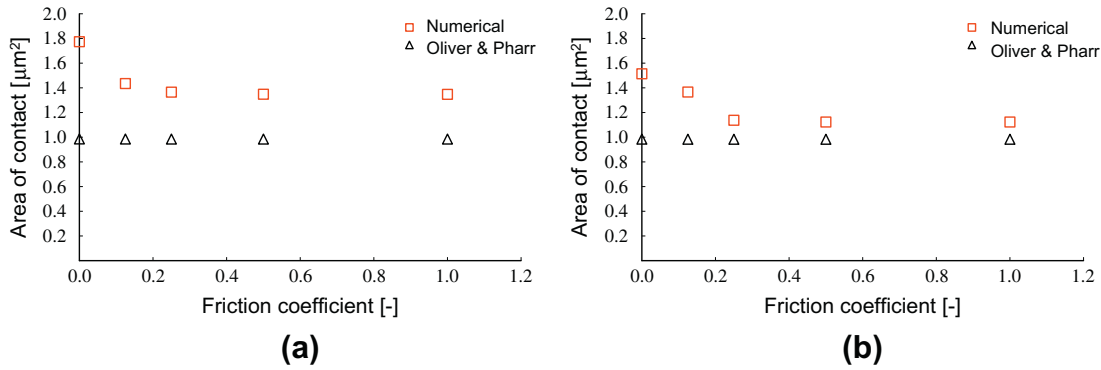
Fig. 5. Area of contact as obtained using the Oliver and Pharr method and numerical techniques for (a) LD C–S–H and (b) HD C–S–H.
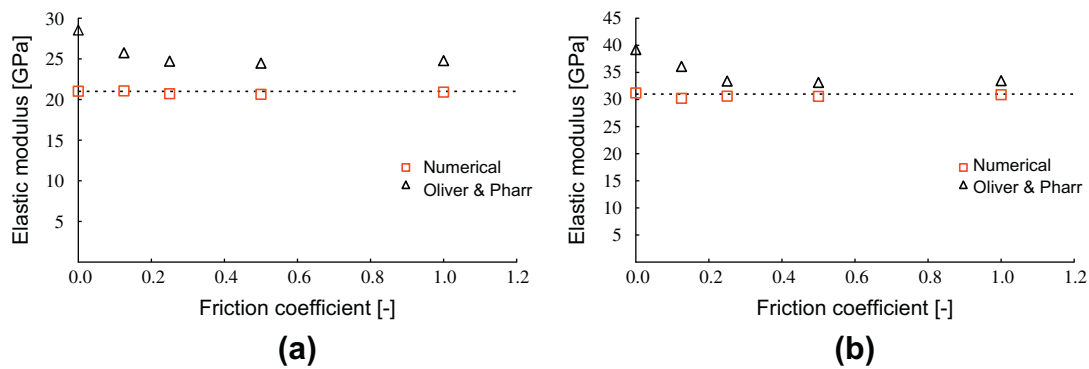

Fig. 6. Elastic moduli of (a) LD C–S–H and (b) HD C–S–H, as calculated using area estimations of the Oliver and Pharr and numerical methods, for various friction coefficients.

consequence for the strength estimation of the C–S–H. The hardness for LD C–S–H and HD C–S–H as calculated using the Oliver and Pharr ($H_{O\&P}$) and numerical estimations (H_{num}), are shown in Fig. 7.

The $H_{O\&P}$ values appear to be insensitive to frictional effects, due to the inability of the method to capture pile-up phenomena, whereas hardness values calculated based on A_{num} (H_{num}) appear to increase as the friction coefficient increases. This is a consequence of several simultaneously occurring phenomena. Firstly, the area of contact reduces as the interface friction increases (see Section 3.2 and Fig. 5), which augments the hardness calculation. Furthermore, a more detailed observation to the evolution of the plastic zone for various μ suggests that as μ increases the volume of the plastic zone also increases leading to an increased H. Fig. 8 shows the plastic equivalent strain (ε^{pl}) that develops in a LD

C–S–H in the case of a contact friction ($\mu = 0.25$) and a frictionless case ($\mu = 0$). In the computations performed, the plastic zone boundaries are computed numerically and are exactly derived from the numerical solution. The definition of the equivalent plastic strain for the Mohr–Coulomb failure criterion is defined as:

$$\bar{\varepsilon}_{pl} = \frac{1}{c} \int \sigma : d\varepsilon_{pl} \tag{7}$$

Fig. 4b shows the distribution of the normal pressure within the contact region. It appears that the increase in contact friction tends to flatten the contact pressure distribution which approached the hardness value (H_{num}) as $\mu > 0.25$. Overall, the results suggest that indentation hardness values are dependent on the extent of interface friction, which should be taken into consideration when analyzing experimental data. Furthermore, in occasions where
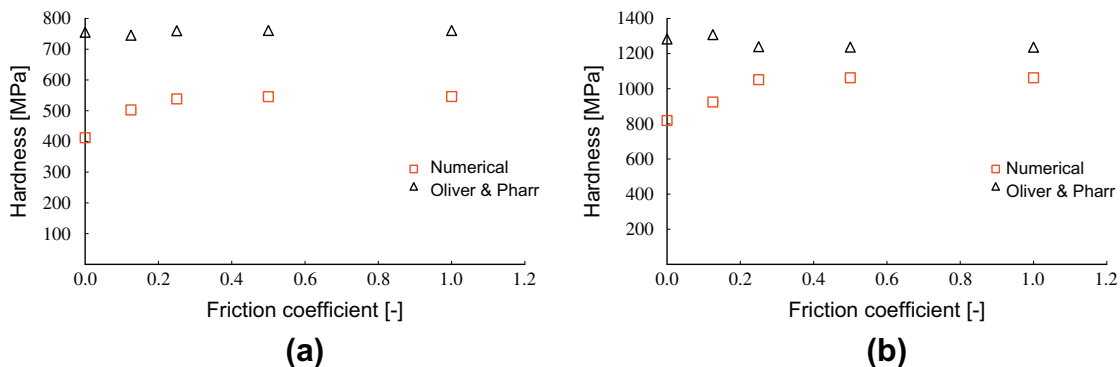

Fig. 7. Hardness values of the (a) LD C–S–H and (b) HD C–S–H, as calculated using the Oliver and Pharr and numerical methods for various friction coefficients.
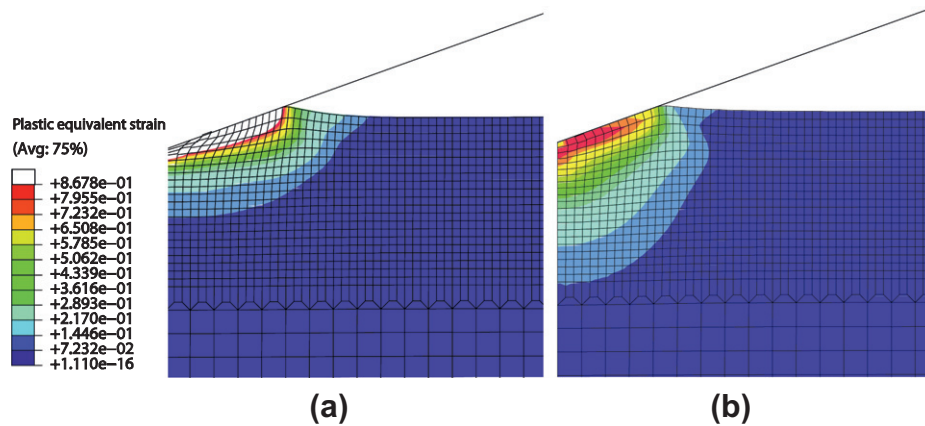
Fig. 8. Effect of contact friction on the extent of the plastic zone. (a) LD C–S–H with $\mu = 0$ (sample A0) and (b) LD C–S–H with $\mu = 0.25$ (sample A2).
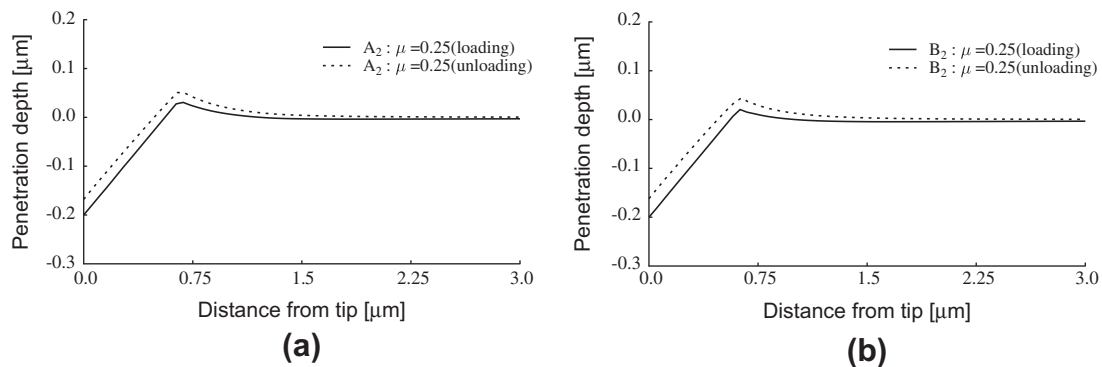

Fig. 9. Displacement profiles in the loaded and unloaded configuration. (a) LD C–S–H with $\mu = 0.25$ (sample A2) and (b) HD C–S–H with $\mu = 0.25$ (sample B2). The projected area of contact remains unaffected.

significant pile-up is present the area of contact as estimated through the Oliver and Pharr method (Eq. (6)) can incorporate uncertainty in the hardness calculation.

3.5. Implications for C–S–H indentation testing

Results presented above suggest that the interface friction can affect the extent of pile-up in C–S–H indentation and as a consequence interfere with the mechanical property extraction process. To quantify this effect on already reported data one will require the experimental determination of the friction coefficient between the indenter (usually diamond) and C–S–H. The majority of the experimental data presented in the literature is performed with a diamond indenter of the three-sided pyramidal, also known as Berkovich, geometry. Recent nano-scratch experiments on cementitious materials report coefficients of friction between a Berkovich (diamond) indenter and the hydration products (C–S–H, Calcium Hydroxide, etc.) on the order of 0.35–0.40 [25]. This value seems reasonable given the coefficient of friction that is commonly experienced between polished metals and diamond indenters, $\mu = 0.2$ [9]. Based on our simulations we conclude that the already reported elastic moduli of the two types of C–S–H are accurate within +17% for the LD C–S–H and +7% for the HD C–S–H. It appears that both experimental values are slightly overestimated. On the other hand hardness data on C–S–H should be treated with additional sensitivity as the effect of friction can affect its magnitude through changes in the area of contact but also on the extend of the plastic zone. Deviations might range from a few percent to a few tens of

percent. The discrepancy caused by the miscalculation of the area of contact due to pile-up phenomena and contact friction might be a reason for the range of hardness data reported in the literature. The error incorporated through the miscalculation of the area of contact can be avoided by observing the residual imprint left on the surface after load removal. Fig. 9 shows the displacement profiles for the loaded and unloaded configurations for samples A2 and B2. The recovery process follows a radial strain discharge mode in which the projected area of contact remains almost unchanged. For all contact friction tested within this paper determination of the area of contact through observation of the residual imprint provides values of A which are within ±10% to the ones determined numerically.

4. Concluding remarks

The effect of contact friction on the nanoindentation measurements of C–S–H has been quantified through finite element simulations. The C–S–H phase has been modeled assuming a linear elastic, cohesive-frictional plastic, material. We showed that the existence of contact friction can affect the extent of pile-up that these materials might exhibit and it is therefore important to include friction in inverse application of simulations for materials property extraction. The elastic moduli of LD and HD C–S–H reported in the literature are within +15%, whereas hardness values might deviate up to +50%. Direct observation of residual imprints can eliminate the largest portion of the area of contact uncertainty, even when contact friction is present. The present calculations

could be revisited to include more advanced constitutive relations for C–S–H (time-dependent deformation, yield-criteria for porous materials, hardening phenomena, etc.) as our understanding of these phases gets more refined.

Acknowledgments

References

[1] Oliver WC, Pharr GM. An improved technique for determining hardness and elastic modulus using load and displacement sensing indentation experiments. J Mater Res 1992;7:1564–83.

[2] Oliver WC, Pharr GM. Measurement of hardness and elastic modulus by instrumented indentation: advances in understanding and refinements to methodology. J Mater Res 2004;19(1):3–20.

[3] Constantinides G, Ulm F-J, van Vliet KJ. On the use of nanoindentation for cementitious materials. Mater Struct 2003;36(205):191–6. Special issue of Concrete Science and Engineering.

[4] Ganneau FP, Constantinides G, Ulm F-J. Dual-indentation technique for the assessment of strength properties of cohesive-frictional material. Int J Solids Struct 2006;43:1727–45.

[5] Cariou S, Ulm F-J, Dormieux L. Hardness – packing density scaling relations for cohesive-frictional porous materials. J Mech Phys Solids 2008;56(3):924–52.

[6] Giannakopoulos AE, Larsson PL. Analysis of pyramid indentation of pressure-sensitive hard metals and ceramics. Mech Mater 1997;25(1):1–35.

[7] Borodich FM, Keer LM. Evaluation of elastic modulus of materials by adhesive (no-slip) nano-indentation. Proc Roy Soc London A – Mater 2004;460(2042):507–14.

[8] Borodich FM, Keer LM. Contact problems and depth-sensing nanoindentation for frictionless and frictional boundary conditions. Int J Solids Struct 2004;41(9–10):2479–99.

[9] Mata M, Alcala J. The role of friction on sharp indentation. J Mech Phys Solids 2004;52:145–65.

[10] Adam CJ, Swain MV. The effect of friction on indenter force and pile-up in numerical simulations of bone nanoindentation. J Mech Behav Biomed 2011;4:1554–8.

[11] Constantinides G, Ulm F-J. The effect of two types of C–S–H on the elasticity of cement-based materials: results from nanoindentation and micromechanical modelling. Cem Concr Res 2004;34(1):67–80.

[12] Constantinides G, Ulm FJ. The nanogranular nature of C–S–H. J Mech Phys Solids 2007;55(1):64–90.

[13] Modal P, Shah SP, Marks L. A reliable technique to determine the local mechanical properties at the nanoscale for cementitious materials. Cem Concr Res 2007;37:1440–4.

[14] Shah SP, Konsta-Gdoutos MS, Metaxa ZS, Mondal P. Nanoscale modification of cementitious materials. In: Bittnar Z, Bartos PJM, Nemecek J, Smilauer V, Zeman J, editors. Nanotechnology in construction 3. Proceedings of the third international symposium on nanotechnology in construction. Springer; 2009. p. 125–30.

[15] Ulm F-J, Vandamme M, Jennings HM, Vanzo J, Bentivenga M, Krakowiak KJ, et al. Does microstructure matter for statistical nanoindentation techniques? Cem Concr Compos 2010;32:92–9.

[16] Vandamme M, Ulm FJ, Fonollosa P. Nanogranular packing of C–S–H at substoichiometric conditions. Cem Concr Res 2010;40(1):14–26.

[17] Pichler Ch, Lackner R. Identification of logarithmic-type creep of calcium–silicate–hydrates by means of nanoindentation. Strain 2009;45(1):17–25.

[18] Nemecek J, Kabele P, Bittnar Z. Nanoindentation of cement pastes and its numerical modeling. In: Kompis V, editor. Conference: conference on composites with micro and nanostructure computational modelling and experiments. Springer; 2008. p. 28–31.

[19] Davydov D, Jirasek M. Modeling of Nanoindentation by a visco–elastic porous model with application to cement paste. In: Bittnar Z, Bartos PJM, Nemecek J, Smilauer V, Zeman J, editors. Nanotechnology in construction 3. Proceedings of the third international symposium on nanotechnology in construction. Springer; 2009. p. 187–92.

[20] Fonseca PC, Jennings HM, Andrade JE. A nanoscale numerical model of calcium silicate hydrates. Mech Mater 2011;43:408–19.

[21] Constantinides G, Ravichandran KS, Ulm F-J, van Vliet KJ. Grid indentation analysis of composite microstructure and mechanics: principles and validation. Mater Sci Eng A – Struct 2006;430(1-2):189–202.

[22] Jennings HM. A model for the microstructure of calcium silicate hydrate in cement paste. Cem Concr Res 2000;30(1):101–16.

[23] Constantinides G, Ulm F-J. The elastic properties of calcium leached cement pastes and mortars: a multi-scale investigation. MIT CEE Report R02-01; 2006.

[24] Constantinides G, Silva ECC, Blackman GS, van Vliet KJ. Dealing with imperfection: quantifying potential length scale artefacts from nominally spherical indenter probes. Nanotechnology 2007;18(30):305503.

[25] Xu J, Yao W. Nano-scratch as a new tool for assessing the nano-tribological behaviour of cement composite. Mater Struct 2011;44:1703–11.